# Debris flow impact on flexible barrier: effects of debrisbarrier stiffness and flow aspect ratio

SONG Dong-ri¹,² https://orcid.org/0000-0001-6892-9770; e-mail: drsong@imde.ac.cn

ZHOU Gordon G. D.¹,²\* https://orcid.org/0000-0001-9014-2931; e-mail: gordon@imde.ac.cn

CHOI Clarence Edward³,⁴ https://orcid.org/0000-0002-9712-1524; e-mail: ceclarence@ust.hk

ZHENG Yun⁵ https://orcid.org/0000-0001-6375-6815; e-mail: yzheng@whrsm.ac.cn

- 1 Key Laboratory of Mountain Hazards and Earth Surface Process/Institute of Mountain Hazards and Environment, Chinese Academy of Sciences, Chengdu 610041, China
- 2 University of Chinese Academy of Sciences, Beijing 100049, China
- 3 Department of Civil and Environmental Engineering, Hong Kong University of Science and Technology, Clear Water Bay, Kowloon, Hong Kong SAR, China
- 4 The HKUST Jockey Club Institute for Advanced Study, Hong Kong SAR, China
- 5 State Key Laboratory of Geomechanics and Geotechnical Engineering, Institute of Rock and Soil Mechanics, Chinese Academy of Sciences, Wuhan 430071, China

Citation: Song DR, Zhou GGD, Choi CE, et al. (2019) Debris flow impact on flexible barrier: effects of debris-barrier stiffness and flow aspect ratio. Journal of Mountain Science 16(7). https://doi.org/10.1007/s11629-018-5314-6

© Science Press, Institute of Mountain Hazards and Environment, CAS and Springer-Verlag GmbH Germany, part of Springer Nature 2019

**Abstract:** Conventionally, flexible barriers are rated based on their ability to resist a free-falling boulder with a particular input energy. However, there is still well-accepted approach for performance of flexible barrier under debris flow impact. In this study, a large-nonlinear finite-element model was used to back-analyze centrifuge tests to discern the effects of impact material type, barrier stiffness, and flow aspect ratio (flow height to flow length) on the reaction force between the impacting medium and flexible barrier. Results show that, in contrast to flexible barriers for resisting rockfall, the normal impact force induced by the highly frictional and viscous debris is insensitive to barrier stiffness. This is because the elongated distributions of kinetic energy are mainly dissipated by the internal and boundary shearing, and only a small portion is forwarded to the barrier. Furthermore, a new stiffness

Received: 27-Nov-2018 Revised: 24-Mar-2019 Accepted: 08-May-2019 number is proposed to characterize the equivalent stiffness between a debris flow or a boulder, and a flexible barrier. Under the circumstance of an extremely elongated debris flow event, *i.e.*, low aspect ratio, the load on a barrier is dominated by the static component and thus not sensitive to the barrier stiffness.

**Keywords:** Debris flow; Flexible barrier; Impact; Stiffness; Flow aspect ratio

#### Introduction

Flexible barriers are commonly installed in mountainous regions to catch rock fragments and boulders. A typical flexible barrier comprises a net suspended by cables and posts. Energy dissipating devices are installed on the cables and are principally responsible for attenuating the impact

<sup>\*</sup>Corresponding author

load (Wendeler et al. 2006, 2007). The barrier stiffness, more specifically, the cable stiffness (along the retaining cable), is the key feature of a flexible barrier. The rockfall flexible barriers are rated based on their capacity to resist a free-falling boulder with a particular input energy (energy approach, EOTA 2016). Over the past decades, flexible barriers designed for rockfall have been hit by debris flows and these barriers have proven to be quite effective (Brighenti et al. 2013; Canelli et al. 2012; DeNatale et al. 1999; Kwan et al. 2014; Wendeler 2008). More and more flexible barriers are now being installed for mitigating debris flows. In contrast to the concentrated rockfall impact, open hillslope landslide or channelized debris flow impact is a distributed and progressive loading process (Major 1997). To account for the difference in loading behavior, GEO (2012) recommended using an energy reduction factor of 0.75 when downscaling a rockfall barrier for resisting open hillslope landslide or channelized debris flow. However, the energy approach cannot provide details like impact pressure and cable force (known as force approach) which are instrumental for the flexible barrier and barrier foundation design (Song et al. 2019). There is certainly a need to better understand the mechanisms of debris impacting a flexible barrier to optimize flexible barrier systems based on the force approach.

Insight on the impact mechanisms between debris flows and a flexible barrier has been hindered by the poor temporal predictability of natural debris flow events (Kwan et al. 2014; Ma et al. 2013; Wendeler et al. 2006; 2007; Chen et al. 2013) and the costly nature of large-scale testing (Bugnion and Wendeler 2010; DeNatale et al. 1999). Furthermore, the vagaries of the natural setting and soil material involved render largescale tests and field monitoring results less reproducible (Iverson 1997; 2015; Iverson and George 2014; Zhang 1993). Bugnion and Wendeler (2010) carried out a series of large-scale tests to model 50 m<sup>3</sup> of debris flows impacting a 3.5-m-tall flexible barrier installed at the end of a 40-m-long natural channel. Findings provided insight on the relevance of hydrodynamic models on estimating the impact force exerted by a debris flow on a flexible barrier. However, details on the response of the energy dissipating devices were not available, which limits a comprehensive understanding of the

effects of flexible barrier stiffness on the resisting forces required.

In this study, the response of flexible barrier cables under concentrated and distributed loading is compared to reveal the fundamental differences between boulder and debris impact. Centrifuge tests (Ng et al. 2016b) were then adopted to calibrate and verify a nonlinear numerical model. A systematic parametric study using the calibrated numerical model was carried out to investigate the effects of debris type, debris-barrier stiffness, and aspect ratio of flow on flexible barrier response. The cable stiffness is adopted as a basic barrier stiffness to non-dimensionalize the results and highlight the correlation between the barrier property and reaction force. This study aims to shed light on the mechanisms of debris-flexible barrier interaction and to provide scientific approach to streamline engineering design.

### 1 Concentrated and Distributed Loading

To reveal the fundamental difference between boulder and debris impact on a flexible barrier, this section compares the response of a single flexible barrier cable, i.e., cable deflection and cable forces, under concentrated and distributed loading. Figures 1a and 1b show schematics (plan view) of a flexible barrier cable with an initial length of L under a point load F and distributed load p. The point load F is assumed to be equal to the product of distributed load p and initial cable length L, i.e., F = pL. The point load F is applied at the middle of cable and the deformed cable is represented linearly. By contrast, the distributed load p is applied uniformly and orthogonally to the cable and its deformed profile is characterized as a circular curve (Sasiharan et al. 2006).

The decomposition of the cable force T includes a component normal to the barrier face  $T_{\rm I}$  and a horizontal component  $T_{\rm H}$  (Figures 1a and 1b). The normal components  $T_{\rm I}$  on the right and left sides of a flexible barrier cable give the impact load F induced by the flow. While the horizontal components  $T_{\rm H}$  on both sides counterbalance each other since they are same in magnitude but in opposite directions.

The maximum deflection  $D_N$  and cable force  $T_N$  resulting from the normal impact load  $F_N$  under

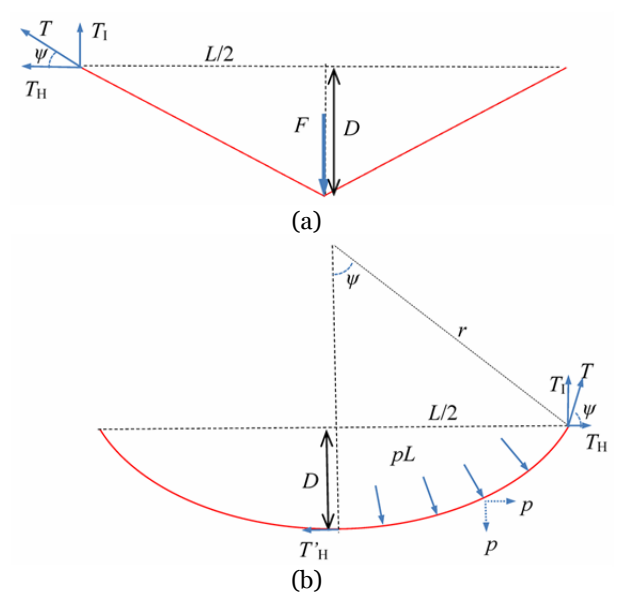


**Figure 1** Schematics of impact load on a horizontal cable under (a) concentrated load F; (b) distributed debris load pL=F along the chord of a circular curve. D is the maximum deflection;  $T'_H$  is the horizontal component of cable force in the middle of cable; r is the radius of the circle.

quasi-static conditions for both the point (concentrated) and distributed loading cases are shown in Figure 2a. Details of the calculation for point load and distributed loading cases are summarized in Appendixes 1 and 2, respectively. The subscript "N" denotes the variables are nondimensionalized by proper normalization. A comparison of deflection  $D_N$  and normal impact load  $F_{\rm N}$  profiles show that the distributed loading case results in a stiffer response compared to the concentrated loading case. More specifically, at  $D_{\rm N}$ = 0.6, the  $F_N$  resulting from distributed loading is 2.3 times of that of the concentrated loading case. On the contrary, the cable force  $T_N$  induced by the distributed loading is lower than that of the concentrated loading (Figure 2a). This is because the deflection angle  $\psi$  for distributed loading is larger than concentrated loading (Figure 2b), leading to a lower induced cable force  $T_N$ .

The stiffer loading response while maintaining lower cable force are the key features of distributed loading. Based on these features, any flexible barrier capable of redistributing concentrated load across the barrier width is beneficial for the flexible barrier structural integrity. Note that the above discussion is based on the same normal impact loads F of concentrated and distributed loading, *i.e.*, under quasi-static loading condition. For dynamic

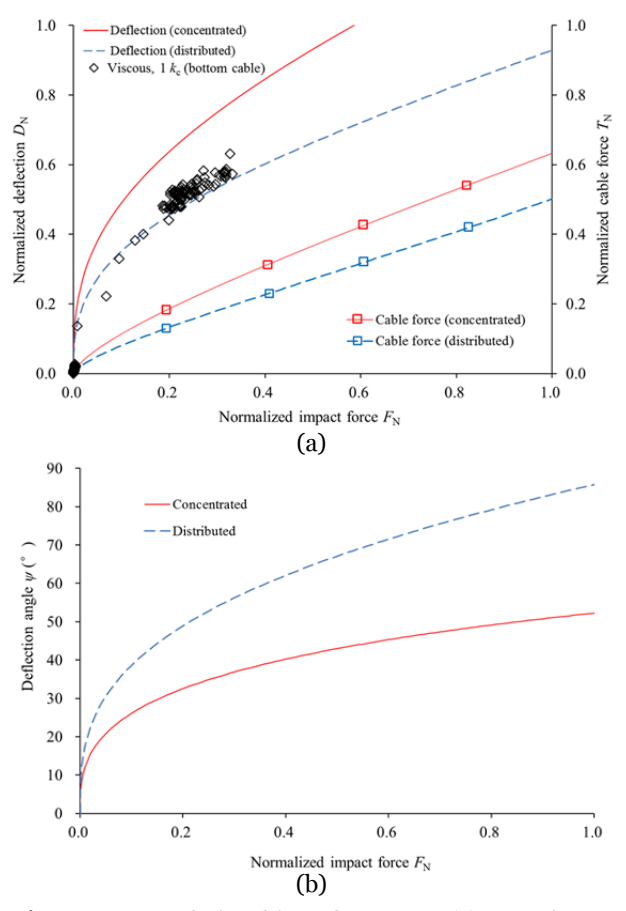


**Figure 2** Relationships between (a) maximum deflection and normal impact load, and cable force and normal impact load; data points of "viscous, 1  $k_c$ " will be discussed in Section "5.2 Cable forces"; (b) impact load and cable deflection angle. The variables are normalized and marked as "N" in the subscript.

scenario, the normal impact load F is a result of boulder or debris impact with certain momentum. Assume a flexible barrier is under separate impact of boulder or debris with the same momentum. Based on the conservation of momentum, a stiffer (distributed) loading response results in a higher impact load, which in turn increases the cable force. Hence the lower cable force as a feature for distributed loading may not be valid for dynamic impact. The sensitivity of flexible barrier response to debris impact with distributed momentum and boulder impact with concentrated momentum will be examined in details below.

#### 2 Flow Characterization

Scaling ensures similarity between the model

and the prototype (Iverson 2015). The Froude number (Fr) governs the dynamics of open channel flows (Choi et al. 2015). In this study, two Fr with different characteristic lengths are defined to quantify the macroscopic flow regimes (Figure 3), specifically, the height Froude number  $Fr_h$  and the length Froude number  $Fr_h$ . The  $Fr_h$  is the ratio between the inertial and gravitational forces acting on the channelized flow and is given as follows:

$$Fr_{\rm h} = \frac{v}{\sqrt{gh}} \tag{1}$$

where v is flow velocity (m/s), g is gravitational acceleration (9.81 m/s²), and h is the flow depth (m). The  $Fr_h$  has been well-established to govern the prevailing impact mechanisms of channelized flows (Armanini et al. 2011; Hübl et al. 2009; Vagnon and Segalini 2016). To provide a clearer physical representation pertaining to the anticipated impact load (Faug 2015), the  $Fr_h$  can be further rearranged as follows:

$$Fr_{\rm h}^2 = \frac{v^2}{gh} = \frac{\rho v^2 hL}{\rho gh^2 L} = \frac{\text{Inertial force}}{\text{Gravitational force}}$$
 (2)

where hL is the impact area on the barrier.

The length Froude number ( $Fr_1$ ) characterizes ratio between the flow velocity v and the free-fall velocity  $\sqrt{gl}$  (Iverson et al. 2014). Alternatively, the  $Fr_1$  is a ratio of time scales for debris motion under gravity  $\sqrt{l/g}$  and debris with length l passing a point l/v:

$$Fr_{1} = \frac{v}{\sqrt{gl}} = \frac{\sqrt{\frac{l}{g}}}{\frac{l}{v}}$$
(3)

 $= \frac{\text{Time of debris motion under gravity}}{\text{Inertial time of debris pass a point}}$ 

Note that in dimensional analysis, physical processes are usually simplified and dimensionless constants can be neglected. For instance, the free-fall velocity  $\sqrt{gl}$  is used to represent the downward debris motion along the slope (Iverson 2015) in Eq. 3.

The ratio of the two Fr in Eqs. 2 and 3 gives an aspect ratio  $\varepsilon$  of a flowing mass (Figure 3):

$$\frac{Fr_{\rm l}^2}{Fr_{\rm h}^2} = \frac{h}{l} = \varepsilon \tag{4}$$

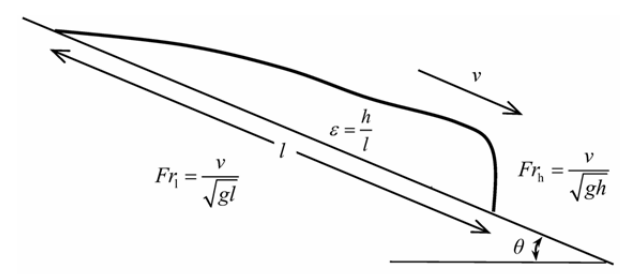


**Figure 3** Schematic vertical cross section of a debris flow surge. Relationship between the height Froude number  $Fr_h$ , length Froude number  $Fr_h$ , and aspect ratio

The aspect ratio  $\varepsilon$  reflects the shape factor of a particular debris flow. A debris flow with a high  $\varepsilon$  can be characterized as a short and thick flow. Such flows carry more momentum at flow front and generate a higher peak impact force compared to a flow with low  $\varepsilon$ , which characterizes an elongated and thin flow body (Ashwood and Hungr 2016; Ishikawa et al. 2010). The aspect ratio is a key factor for the design of debris flow protection structure and more details are discussed in Section "6.4 Effects of flow aspect ratio".

# 3 Centrifuge Modelling of Debris Flows Impact on Flexible Barrier

A series of centrifuge model tests (Ng et al. 2016b) using dry sand and viscous fluid flows separately were back-analyzed. The centrifuge tests were carried out at a gravitational acceleration of 22.4g. A model flexible barrier, equivalent to a 5.2 m (233 mm in model scale) wide and 4.5 m (200 mm in model scale) high barrier in prototype, was installed perpendicularly to a 25° slope. The new flexible barrier model comprises four instrumented cables controlled using spring mechanisms to replicate the non-linear cable response (Chan et al. 2012) of a prototype flexible barrier using a simplified bilinear loading curve (Ng et al. 2016a). An impermeable barrier was adopted to prevent debris from passing and to isolate the effects of barrier stiffness (Leonardi et al. 2016). In the impact process, the displacement and force of spring mechanisms are scaled by 1/N and  $1/N^2$ times, respectively. Thus, the stiffness of flexible has a scaling factor of 1/N. The well-established scaling laws (Bowman et al. 2010; Ng et al. 2016a; Schofield 1980) for the impact problem are

summarized in Table 1. Details of the centrifuge tests are discussed in Ng et al. (2016b).

Table 1 Relevant scaling laws

Parameter	Dimension	Scaling law (model/prototype)
Gravity	$L/T^2$	N
Density	$M/L^3$	1
Length (displacement)	L	1/N
Mass	M	$1/N^3$
Velocity	L/T	1
Inertial time	T	1/N
Force (impact load)	$ML/T^2$	$1/N^2$
Flexible barrier stiffness	$M/T^2$	1/N

Load cells were installed along each horizontal cable to measure the induced axial force. Laser sensors were used to capture the elongation of the cable of model barrier. The cable displacement and force measurements were captured synchronously. The interaction kinematics was captured using a high-speed camera. The velocity attenuation and impact mechanisms behind the barriers were analyzed using Particle Image Velocimetry (PIV) analysis (Take 2015; White et al. 2003).

Leighton Buzzard fraction C sand was used to model dry granular flows. The sand comprises fairly uniform grains with diameters of about 0.6 mm. The bulk density of the material held within the storage container was about 1530 kg/m³. The internal friction angle of the sand is 31°. The viscous liquid has a density of 1580 kg/m³ and a measured specific viscosity of 11.3 Pa·s. The high viscosity of real debris flows is attributed to the high solid fraction of debris flows. The prototype volume of the debris is 250 m³ (22 Liter in model scale).

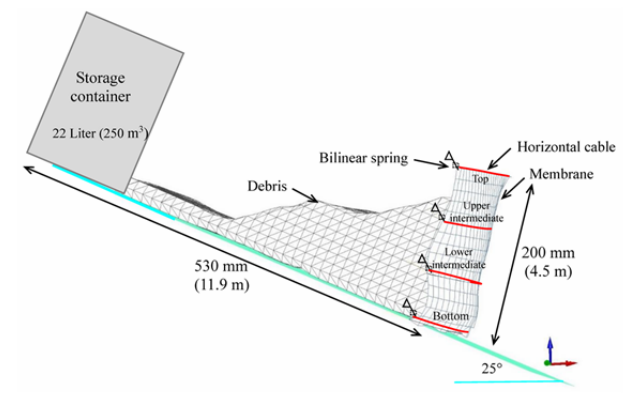
# 4 Large-nonlinear Finite Element Modelling of Debris and Boulder Impact on Flexible Barrier

The most commonly adopted approaches for modelling debris flow are based on depth-averaged continuum models (Iverson and George 2014). Continuum models are robust and very computationally efficient. The advantages of 3D continuum approach include its ability to allow for vertical momentum transfer and thus to model debris flow impact problems, *i.e.*, debris run-up and dead zone formation. In this study, 3D large-nonlinear finite element software package, LS-

DYNA, was adopted for back-analyzing the centrifuge tests and carrying out a parametric study. LS-DYNA uses an explicit time integration to study nonlinear flow problems and has been widely used for stress and deformation analysis of structures subjected to impact (Hallquist 2007). Arbitrary Lagrangian-Eulerian formulation discretizes the computational domain into a mesh of elements (Donea et al. 1982), which can move arbitrarily and optimize its shape to distortion, thereby enabling prevent deformation to model debris flow. The numerical model has been verified against several welldocumented case studies, including Yu Tung Road debris flow in Hong Kong (AECOM 2012; Kwan et al. 2015).

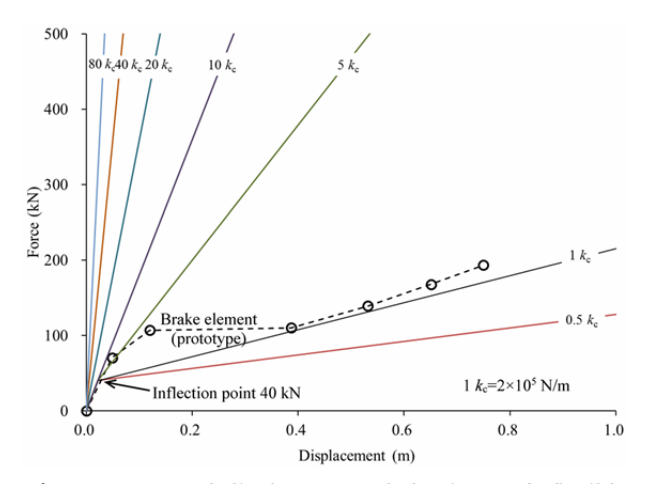
#### 4.1 Numerical model setup

Figure 4 shows the three-dimensional finite element mesh adopted in this study. The barrier face (membrane, shell element), horizontal cables (beam element), slope bed (shell element), container (shell element), and the boulder (solid element) were based on the Lagrangian description (Leonardi et al. 2016). To solve numerical problem of modelling the large deformation of the flow, the was modelled using the Arbitrary Lagrangian-Eulerian (ALE) approach. Debris movements were constrained by the slope bed and the side walls. The brake element (energy dissipating device) was modelled as a bilinear loading behavior (Figure 5). The opening of storage container was calibrated to ensure the released debris achieve the necessary Froude conditions. For tests pertaining to boulder impact, a single elastic ball with a prototype diameter of 2.42 m and



**Figure 4** 3D FEM mesh of numerical model (Prototype dimensions in the bracket).

an initial velocity in front of the flexible barrier was modelled.



**Figure 5** Load-displacement behaviors of flexible barrier horizontal cable with varying stiffness (along the cable direction, all dimensions in prototype scale)

**Table 2** Properties of flexible barrier and debris materials (all dimensions in prototype)

Key items		Parameter	Value	
Debris	Viscous	Density $\rho$	1580 kg/m <sup>3</sup>	
	Viscous	Viscosity $\eta$	11.3 Pa·s	
		Shear modulus G	5.0×10 <sup>5</sup> Pa	
		Bulk modulus K	1.0×10 <sup>6</sup> Pa	
	Frictional	Density $\rho$	1530 kg/m <sup>3</sup>	
		Friction angle $\varphi$	31°	
		Cohesion c	o.1 kPa	
Boulder		Young's modulus E	5.2×10 <sup>10</sup> Pa	
		Poisson's ratio $v$	0.23	
		Density $\rho$	2600 kg/m <sup>3</sup>	
		Diameter d	2.42 m	
Flexible cable		Stiffness $K_1$	$1.8 \times 10^6  \text{N/m}$	
		Stiffness $K_2$ (1 $k_c$ )	2.0×10 <sup>5</sup> N/m	

# **4.2** Constitutive models and model parameters

The rheology of the viscous fluid was described using a viscous model with dynamic viscosity  $\eta$  = 11.3 Pa·s and density of 1580 kg/m³. The dry sand is modelled as a cohesionless medium with friction angle of 31° and its behavior is described by the Drucker-Prager yield criteria with an associated flow rule and assuming constant volume. The dry sand is referred to as "frictional" herein. To prevent numerical instability, a non-zero value of cohesion 0.1 kPa (ARUP 2013; Kwan et al. 2015), which does not pose obvious influence on the flow behavior, was provided. The properties of boulder are equivalent to a granite sphere with elastic modulus

of  $5.2 \times 10^{10}$  Pa and density 2600 kg/m<sup>3</sup>. Table 2 provides a summary of the material properties for this study.

#### 4.3 Flow-barrier contact algorithm

Interaction between the debris (ALE), boulder (solid element), and barrier (membrane, shell element)/slope bed (shell element) is modelled using finite-element contacts. The independent motion of each contact is calculated over a small time step in the order of microseconds (Hallquist 2007). Any penetration of the debris (boulder) into the barrier or channel results in a normal reaction force which is distributed evenly between debris/boulder and the barrier/channel. The magnitude of this force is proportional to the amount of penetration and is determined using an interface spring stiffness governed by an equivalent modulus resulting from the debris/boulder and barrier/slope bed (Koo 2017). In the preparation of centrifuge tests, by using the tilting test method (Hungr 2008), the interface friction angle between channel bed and debris material was calibrated as 22.6°. In the numerical model, Coulomb friction with a coefficient of 0.42 was adopted at the interface between the debris/boulder and the channel.

### 4.4 Numerical modelling procedure

Each simulation subjects the model to the influence of gravity by increasing the gravitational acceleration gradually from 0 to 22.4 g. After reaching the desired g-level, the debris in the storage container is released on to the slope. For the boulder, the initial velocity was set the same as that of the debris flow velocity (12 m/s) before impact. The momentum of the boulder is only 10% that of the viscous and frictional debris flows because the overall volume is less. The impact pressure induced by debris/boulder on the barrier face is further transferred to the cables and the dynamic response is recorded using the beam elements.

# 4.5 Numerical simulation plan

In total 28 numerical simulations were carried out. The focus of this study is to investigate the

response of barrier subjected to distributed debris flow loading (viscous and frictional flow cases) and concentrated boulder loading. Figure 5 shows the bilinear behavior of the cable used to replicate the complex prototype load-displacement response of a flexible barrier. The bilinear behavior of the cable comes from the elasto-plastic load-displacement response of energy dissipating devices attached to the cable (Castanon-Jano et al. 2017). The first stage of the bilinear behavior denotes the elastic deformation of the cable and energy dissipating devices, while the second stage denotes the plastic deformation of the energy dissipating devices. Only the second linear stage of the bilinear response  $(K_2)$ is varied. The reference stiffness  $k_c = 2.0 \times 10^5 \text{ N/m}$ (Table 2; Ng et al. 2016b). The stiffness is varied as  $nk_c$ , where n = 0.5, 1, 5, 10, 20, 40, and 80. A cablestiffness that is equal or greater than 10  $k_c$  is considered as linear rather than bilinear. The cable stiffness marked as "Brake element" is the loading behavior of a brake element from a proprietary prototype flexible barrier (Zhou et al. 2011). In order to obtain a better understanding of the effects of flow aspect ratio on the dynamic response of flexible barrier, the discharge rate of the debris flows was tuned to study a range of aspect ratio ranging from 0.019, 0.020, 0.022, to 0.023. A summary of the parameters investigated is given in Table 3.

# 5 Calibration of Numerical Model

#### 5.1 Impact mechanisms

To compare test results, the initial time of all 28 tests is set to 1.0 s just as the flow front impacts the barrier. All results are presented in prototype. Figure 6 depicts the impact kinematics of a viscous flow impacting a flexible barrier with stiffness 1  $k_c$ . The flow decelerates and jumps along the barrier face, thereby inducing large deformation of the barrier (Figures 6a and 6b). The jump eventually rolls back towards the channel (Figures 6c and 6d). The change in color of the flow demonstrates that the velocity decreases after impacting the flexible barrier. Figure 7 shows a typical comparison of the observed impact kinematics, corresponding Particle Image Velocimetry (PIV) analysis, and the computed impact kinematics (with velocity vectors) for the viscous and frictional flows. The impact of

**Table 3** Summary of parameters considered in the impact on flexible barrier

Parameters	Debris rheology	Cable stiffness $(nk_c)$	$\mathit{Fr}_{\mathtt{h}}$	Aspect ratio $\varepsilon$
Cable stiffness $(nk_c)$	Viscous Frictional Boulder	0.5 1 Brake element* 5 10 20 40 80	3.67	0.019
Flow regime	Viscous	1	3.59 3.62	0.019 0.020 0.022 0.023

<sup>\* &</sup>quot;Brake element" is the loading behavior of a brake element from a proprietary flexible barrier (Zhou et al. 2011).

the viscous flow against the flexible barrier exhibits a pronounced jump, herein referred to as a run-up mechanism. By contrast, the frictional flow develops a pile-up mechanism where sand progressively layers on top of a static deposit (Choi et al. 2015; Wendeler and Volkwein 2015; Wendeler 2016). A comparison of the impact kinematics corroborates that the selected constitutive models and input parameters are capable of capturing key features of viscous and dry sand flows impacting a flexible barrier.

#### 5.2 Cable forces

Figure 8a shows a comparison of the computed and measured axial loads in the top, upper intermediate, lower intermediate, bottom cables. The discrepancy in the top cable is attributed to the difference in time for the debris to reach the top of barrier. To further examine the performance of the numerical model prediction, the computed normal impact force and maximum deflection of the bottom cable are shown in Figure 2a. Although the loading behavior of the model barrier cable, with stiffness 1  $k_c$ , is characterized as bilinear (Figure 5), the computed data for distributed loading shows reasonable agreement with the theoretical prediction. When cable load exceeds the inflection point for the bilinear curve (40 kN), the influence of high stiffness in the first stage of bilinear loading tends to be negligible compared to the low stiffness of the second stage of the loading curve. Comparison of the normal

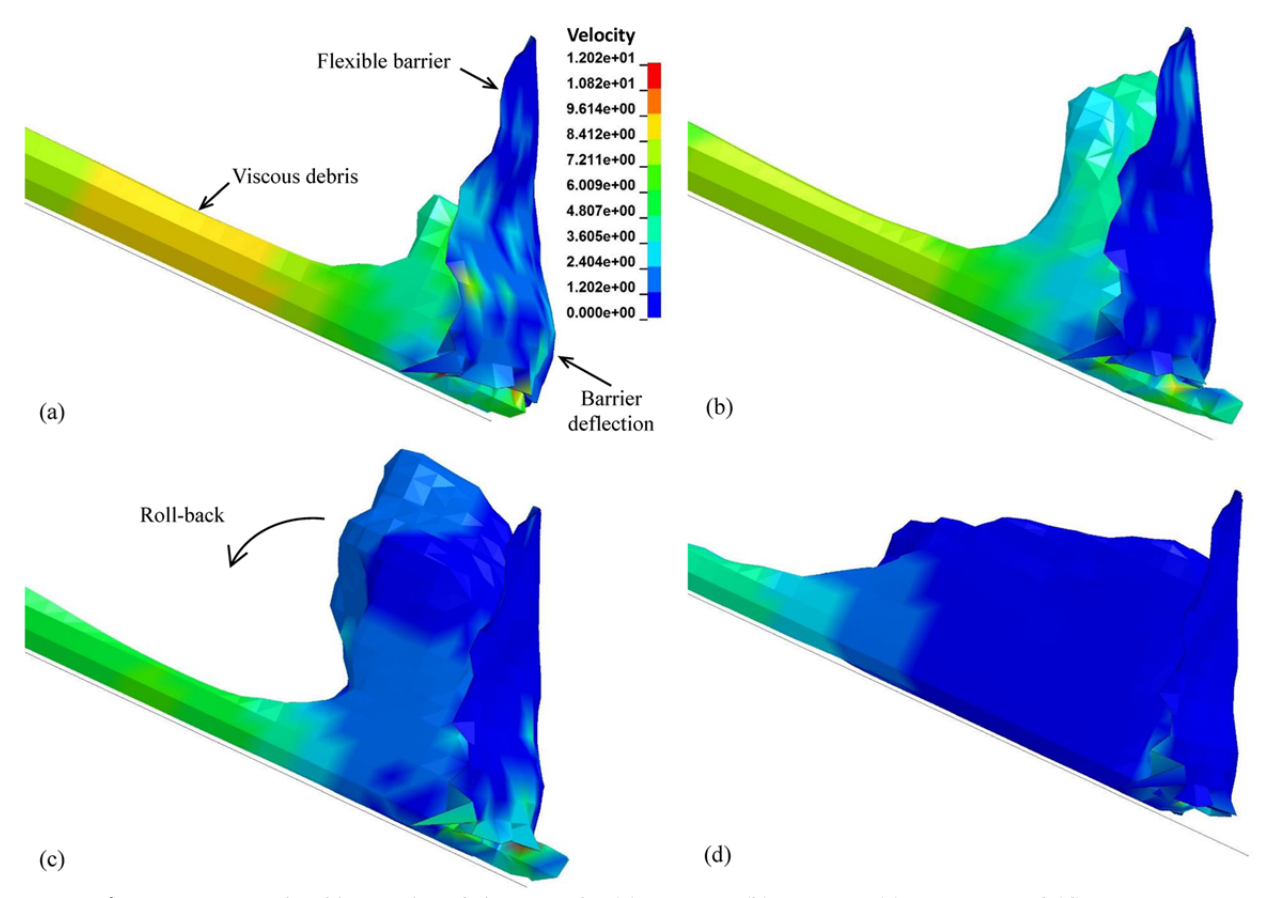


**Figure 6** Interaction kinematics of viscous, 1  $k_c$ : (a) t = 1.3 s; (b) t = 1.8 s; (c) t = 2.3 s; and (d) t = 2.8 s.

impact force for viscous and frictional debris materials shows that the difference between the measured and modelled total force is less than 10% (see Section "6.1 Effects of impact material type").

# 6 Result Interpretation

# 6.1 Effects of impact material type

The forces exerted by the viscous flow impacting a flexible barrier with stiffness 1  $k_c$  are shown in Figure 9a. The computed peak value of the normal impact force F agrees well with that predicted using hydrodynamic equation  $F = \alpha \rho v^2 h L$  ( $\alpha = 1.0$ , WSL 2009). By contrast, the boulder impact force, a shorter duration impact, exhibits a much higher normal peak load (Figure 10a).

Figure 11 shows the response of a flexible barrier with stiffness of 1  $k_c$  impacted by viscous and frictional debris flows and a boulder. The normal impact force resulting from the different materials impacting the flexible barrier is

normalized by the impact force (749 kN) exerted by the viscous flow (Figure 9a). The measured impact forces of the viscous and frictional flows from the centrifuge model tests (Ng et al. 2016b) are also shown for comparison. The impact force exerted by the viscous flow, characterized by a run-up impact mechanism, is almost twice that of the frictional pile-up impact mechanism. Although the boulder only carries 10% of the momentum of the debris flow before impact, the normal impact load (1403) kN) is about twice as much as the viscous flow impact (749 kN). This impact force on flexible barrier is higher than the characteristic value (1000 kN) on rigid structures as recommended by (Austrian Standards Institute 2010; Huebl et al. 2017). This is because the size (2.42 m in diameter) and velocity (12 m/s) of boulder in this study are far beyond the design scenario of ONR 24801 (e.g., boulders of 0.5 m in diameter, 1300 kg in mass, and 9 m/s in velocity, or 1.0 m in diameter, 10000 kg in mass, and 3 m/s in velocity).

Debris-resisting flexible barriers originate from rockfall flexible barriers, but the mechanisms

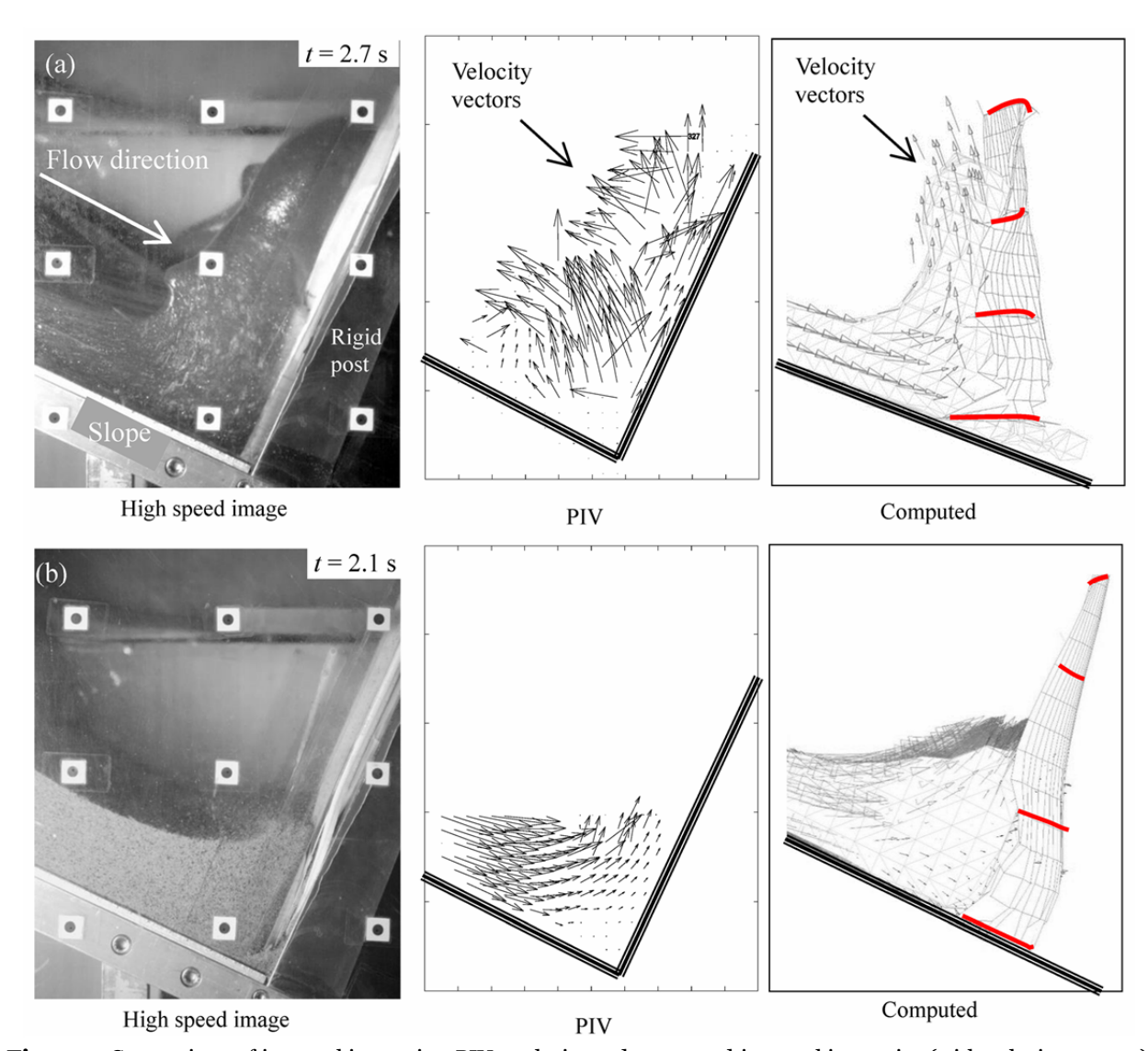


**Figure 7** Comparison of impact kinematics, PIV analysis, and computed impact kinematics (with velocity vectors): (a) Viscous at t = 1.8 s showing run-up mechanism; (b) Frictional at t = 2.1 s, showing pile-up mechanism. The deflection of flexible barrier in the high-speed image was hidden by the rigid post.

that govern the dissipation of energy are quite different. A single boulder exerts a concentrated load on the face of the barrier. The impulse leads to localized deformation and the kinetic energy of the boulder is mainly absorbed by the barrier itself. In contrast, when a debris flow impacts a flexible barrier, there is a significant attenuation of kinetic energy within the flow body itself. A debris flow front may impose an impulse load on the barrier over a distributed area, however subsequent flow is attenuated by interaction with the deposited material in front of the barrier in a relatively mild manner (Moriguchi et al. 2009; Ng et al. 2016b). The kinetic energy is mainly dissipated through the internal shearing enhanced by the velocity gradient

between flowing debris and static deposit (Song et al. 2019). The role of the static deposit is critical to the flexible barrier design. Thus the impact pattern of a distributed load on a single cable (without static load, Figure 1b) cannot fully represent the impact scenario of debris flow interacting with a whole flexible barrier. The discussion of distributed loading induced high impact load in Section 1 "Concentrated and Distributed Loading" is not confirmed by this numerical study. Furthermore, a debris flow with more momentum concentrated on the flow front, as the boulder impact does, could induce larger impact load, because the influence of static deposit is not significant at the frontal impact.

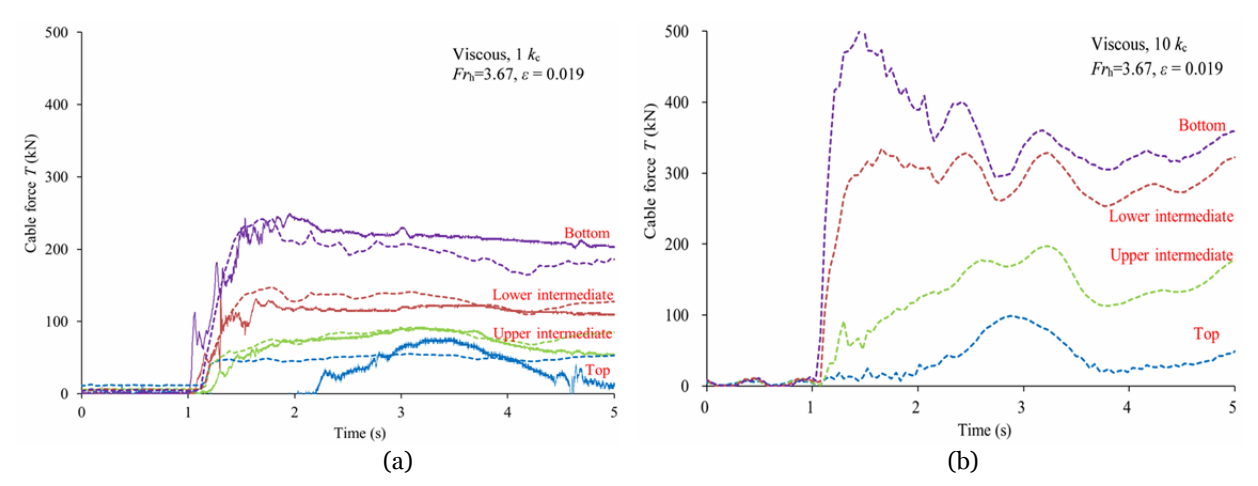


**Figure 8** Comparison of measured and computed cable forces (a) measured (solid lines) and computed axial cable force T for viscous, 1  $k_c$ ; (b) computed axial cable force T for viscous, 10  $k_c$ . (all dimensions in prototype)

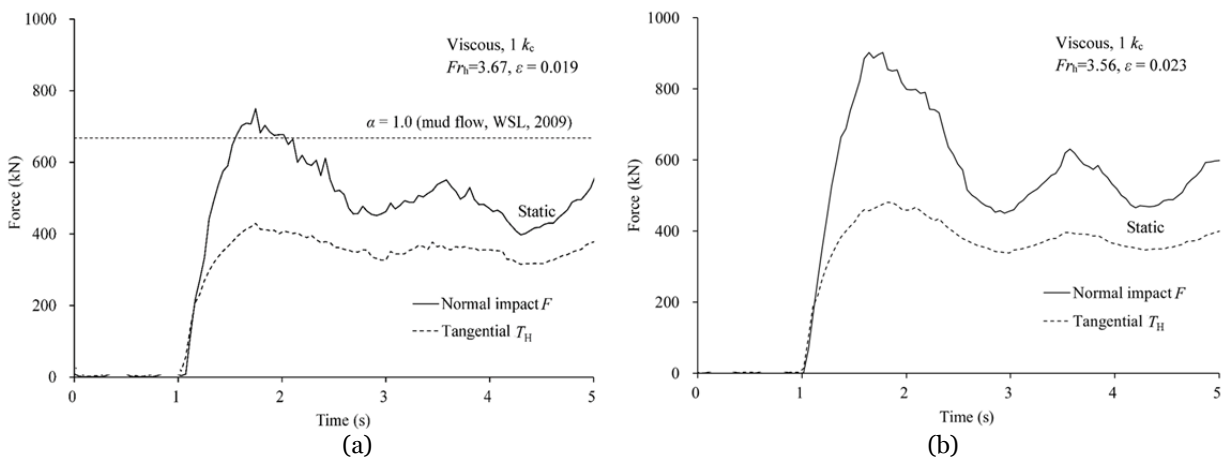


**Figure 9** Total normal impact F and tangential force  $T_H$  time history of viscous, 1  $k_c$  (a)  $\varepsilon$  = 0.019; (b)  $\varepsilon$  = 0.023. The total load goes through several cycles of fluctuation before approaching static. (all dimensions in prototype)

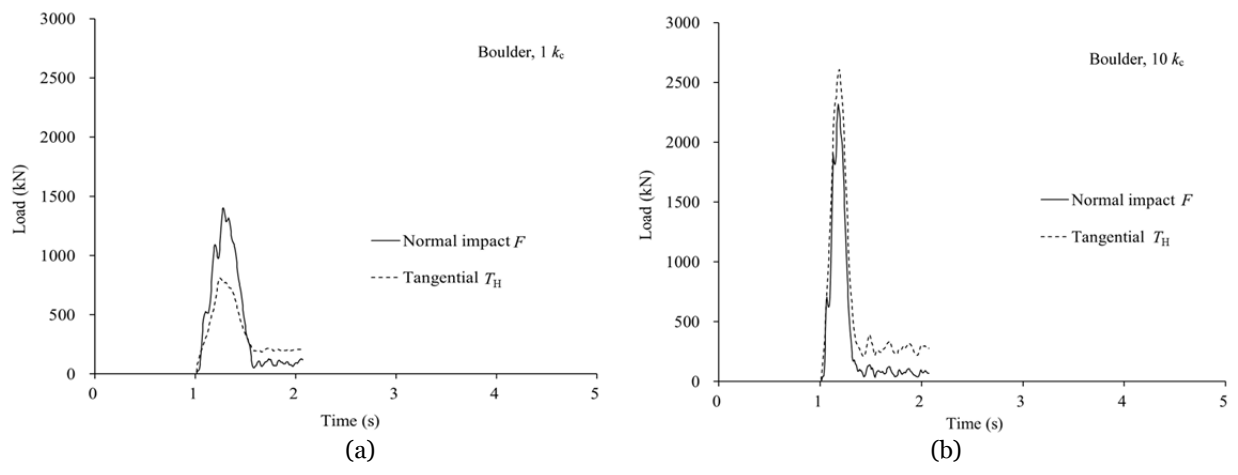


**Figure 10** Total normal impact F and tangential force  $T_H$  time history of boulder impact (a) 1  $k_c$  stiffness; (b) 10  $k_c$  stiffness. (Note the difference in magnitude between Figure 9 and Figure 10; all dimensions in prototype)

### 6.2 Effects of barrier stiffness

Figure 8b shows the change in cable force with time for a viscous liquid impacting a flexible

barrier with a stiffness of 10  $k_c$ . The peak cable force becomes larger as the barrier stiffness increases. The cable force at the bottom cable is more than two times of that on a barrier with stiffness 1  $k_c$ . As expected, the boulder impact load on the flexible barrier induced increase dramatically with barrier stiffness 10  $k_c$  (Figure 10b). More importantly, the tangential force exceeds the normal force. The flexible barrier response is highly sensitive to the cable stiffness, suggesting that cable stiffness may govern the structural integrity of a flexible barrier, for instance, potential failure of cables and anchor foundations.

The influences of cable stiffness and type of material impacting the barrier on the normal impact force exerted on the barrier are shown in Figure 12a. The cable stiffness is varied from 0.5 to 80  $k_c$ . The impact force is normalized by the impact force of viscous flow against a barrier with stiffness of 1  $k_c$ . Neither the normal impact forces of the viscous nor frictional debris flows are sensitive to barrier stiffness. The impact forces only vary by 20% within the range of stiffness investigated in this study. By contrast, the boulder impact force shows high sensitivity to barrier stiffness.

Unlike the normal impact force, the tangential force  $T_{\rm H}$  (refer to Figure 1 for definition) increases with barrier stiffness regardless of the type of material impacting the barrier (Figure 12b). A threefold difference in tangential force is exhibited for viscous debris flow when the stiffness is varied from 1 to 80  $k_c$ . This suggests that an increase in cable force (see Figures 7a and b) is predominantly contributed by the tangential component  $T_{\rm H}$ . This implies an impact load exerted on a flexible barrier is mainly governed by the effects of geometry. More specifically, the different deflection angles that result from different cable stiffness. As one would expect from trigonometry (Figures 1a and b), stiffer cables exhibit smaller deflection, which leads to smaller deflection angles  $\psi$  and larger tangential cable forces (Appendix 2). A softer barrier can reduce the cable force T, despite the normal impact force *F* not being reduced.

Intuitively from the conservation of momentum, one would expect that an increased normal impact force is expected for a stiffer barrier, since the interaction duration is shortened. However, results show that only the tangential force is sensitive to the effect of varying the

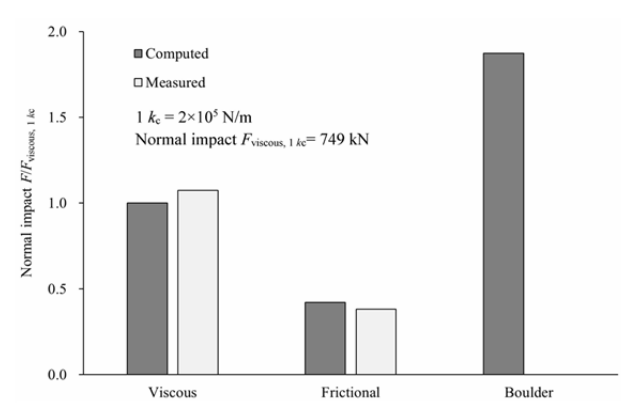


**Figure 11** Comparison of normal impact force F for different debris types at 1  $k_c$  condition.

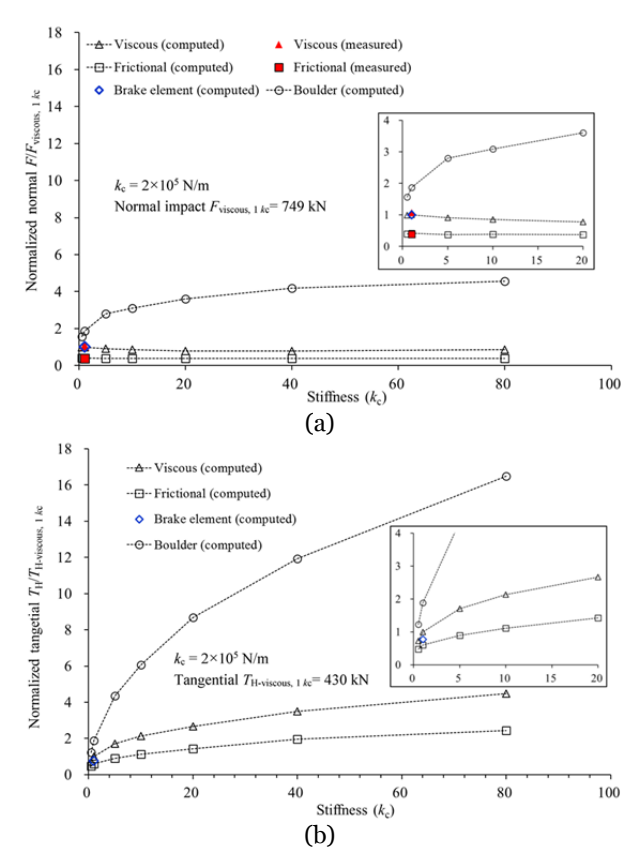


**Figure 12** Stiffness effect on the flexible barrier response: (a) total normal impact force F; (b) total tangential force  $T_{\rm H}$ . Inset figures show the details close to the origin point.

stiffness of the barrier. The normal impact force in this study is remains nearly constant as the stiffness of barrier cable varies from 0.5 to 80  $k_c$ . This finding is consistent with that reported by Ashwood and Hungr (2016). In their numerical simulations, when the deflection is less than 25% of the flow depth, the force is almost constant, thereby mimicking the behavior of a rigid barrier.

The effects of flexibility only exhibit a substantial effect on reducing the impact force when the deflection is close to the flow thickness. However, in this study, even though the deflection is approximately the same as that of the flow depth, the normal impact force still remains constant. The viscous liquid in this study has a high viscosity, denoting a much efficient energy dissipation rate. Subsequently, the computed peak normal impact forces are not that distinct compared to the static loads (Figure 9a), leaving limited space for the flexible barrier to buffer. The influencing factors on the normal impact force are further discussed based on the aspect ratio in Section 6.4 "Effects of Flow Aspect Ratio".

The response of the "Brake element" nonlinear stiffness is very close to that of the barrier with a stiffness of 1  $k_c$  in terms of both normal and tangential forces (Figure 12 a & b). This suggests that the influence of nonlinearity on the load-displacement behavior of the Brake element has a minor effect.

#### 6.3 Equivalent debris-barrier stiffness

Blanco-Fernandez et al. (2016) modelled a twodimensional unstable slope mass impacting a flexible membrane using the SPH method. Results revealed that internal failures inside the unstable mass have more influence on the impact pressure, while the influence of elastic modulus is negligible. Based on this finding, the relative stiffness between the debris and a flexible barrier was proposed as a ratio of the debris flow impact force using the hydrodynamic approach (Kwan 2012; WSL 2009) to the resisting force of the cable once it is fully elongated:

$$R_{\rm D} = \frac{\alpha \rho v^2 h L}{n k_{\rm c} L} \tag{5}$$

where  $\alpha \rho v^2 h L$  is the impact force exerted on an area hL. The relative stiffness can also be regarded using the Johnson Number (Randolph and White 2012), which provides the relative magnitudes of the impact force to the resisting force from a structure. To preserve a clear physical meaning, the variables with same length dimensions, h in the numerator and L in the denominator, have been cancelled out. Also, the dynamic pressure coefficient  $\alpha$  is neglected. The final expression of the stiffness ratio  $R_D$  is a ratio of debris impact

pressure  $\rho v^2$  to the barrier stiffness per unit width  $nk_c/L$ :

$$R_{\rm D} \sim \frac{\rho v^2}{nk_c / L} \tag{6}$$

For a single boulder, the stiffness is characterized as the reaction force under contact and given as follows:

$$R_{\rm B} = \frac{E_{\rm B}}{nk_{\rm c}/L} \tag{7}$$

where  $E_B$  is the Young's modulus of the boulder (Pa).

The combined influence of debris flow and barrier stiffness on the flexible barrier response can be represented as an equivalent stiffness given as follows:

$$S_{\rm D} = \frac{(\rho v^2)(nk_{\rm c}/L)}{\rho v^2 + nk_{\rm c}/L} = \frac{\rho v^2}{R_{\rm D} + 1}$$
(8)

and for boulder impact, the expression is given as follows:

$$S_{\rm B} = \frac{E_{\rm B}(nk_{\rm c}/L)}{E_{\rm B} + nk_{\rm c}/L} = \frac{E_{\rm B}}{R_{\rm B} + 1}$$
(9)

The physical meaning of the equivalent stiffness  $S_B$  is analogous to the equivalent modulus in contact mechanics (Johnson 1985) whereby the two objects in contact both contribute to the overall reaction force. When the barrier is infinitely stiff, the equivalent stiffness becomes  $\rho v^2$ , which is the hydrodynamic expression for fluid impacting a perfectly rigid plate. Under this condition, the normal impact force is governed by the properties of the debris, rather than the barrier. A summary of the values of equivalent stiffness with varying cable stiffness is given in Table 4.

The equivalent stiffness values  $S_D$  and  $S_B$  can be normalized by  $\rho v^2$  to provide a stiffness number for debris flow impact:

$$NS_{\rm D} = \frac{1}{R_{\rm D} + 1} \in (0,1)$$
 (10)

and for boulder impact:

$$NS_{\rm B} = \frac{E_{\rm B} / (\rho v^2)}{R_{\rm B} + 1} \tag{11}$$

**Table 4** Summary of the generalized stiffness (all dimensions in prototype)

$nk_{\mathrm{c}}$	Deb	ris		Boulder			
	$R_{\rm D}$	$S_{\rm D}({\rm kN/m})$	$NS_{\mathrm{D}}$	$R_{\rm B}$	$S_{\rm B}  ({\rm kN/m})$	$NS_{\rm B}$	
0.5	13.3	16.0	0.07	$3.0 \times 10^6$	17	0.1	
1	6.6	29.8	0.13	$1.5 \times 10^{6}$	34	0.2	
5	1.3	97.8	0.43	$3.0{\times}10^{5}$	172	0.8	
10	0.7	136.8	0.60	$1.5 \times 10^{5}$	343	1.5	
20	0.3	170.9	0.75	$7.6 \times 10^5$	687	3.0	
40	0.2	195.2	0.86	$3.8 \times 10^4$	1373	6.0	
80	0.1	210.1	0.92	1.9×10 <sup>4</sup>	2747	12.1	

**Notes:**  $nk_c$ , Stiffness;  $R_D$ , Stiffness ratio of debris;  $S_D$ , Generalized stiffness of debris;  $NS_D$ , Generalized dimensionless stiffness of debris;  $R_B$ , Stiffness ratio of boulder;  $S_B$ , Generalized stiffness of boulder;  $NS_B$ , Generalized dimensionless stiffness of boulder.

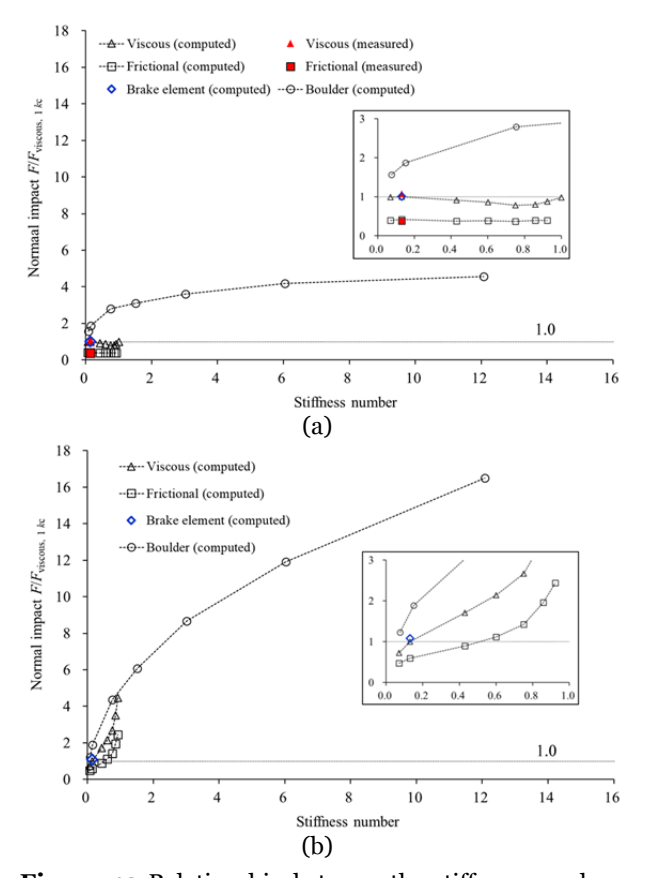


**Figure 13** Relationship between the stiffness number  $(NS_D \text{ and } NS_B, \text{ generalized dimensionless stiffness)}$  and (a) normal impact force F; (b) tangential force  $T_H$ . Inset figures show the details close to the origin point.

Figures 13a and 13b show the relationship between the stiffness number and the normal impact force and the tangential force  $T_{\rm H}$ . For debris flow impact, the cable stiffness, varying from 0.5 to 80  $k_{\rm c}$ , falls within a limited range (0-1) after normalization. In contrast, the stiffness number for

boulder impact covers a much wide range of values as the barrier stiffness increases. The huge contrast in stiffness numbers between debris flow and a boulder implies that debris flow properties affect the flexible barrier response. A summary of the stiffness numbers for both debris flow and boulder impact are given in Table 4. The low sensitivity exhibited by debris impact force to the barrier stiffness can also be explained by narrowing the range of stiffness numbers in Figure 13a. By contrast, the high stiffness of boulder itself leads to a wide range of stiffness numbers. Although this study separates the impact of debris flow and boulders, in reality natural geophysical flows contain both. More importantly, boulders tend to migrate to the front of flows via particle-size segregation (Johnson et al. 2012) and induce large concentrated loads. Flexible barriers in turn can provide a significant attenuating effect on the peak force of boulder-enriched flow fronts.

Due to the effects of geometry, the tangential force for both debris and boulder loading increases with barrier stiffness (Figure 13b). However, the magnitude of the tangential forces resulting from debris loading is limited compared to boulder loading.

#### 6.4 Effects of flow aspect ratio

Boulder impact imposes significantly higher normal impact forces on a flexible barrier. This is mainly attributed to the highly-concentrated momentum acting on the barrier as well as the high stiffness of the boulder itself. By contrast, debris loading imposes progressive and prolonged distribution of momentum on the barrier. Furthermore, during debris impact, subsequent flow is strongly influenced by the previous deposit at the barrier base (see Figure 7). The extent to which momentum is distributed during impact depends on the flow aspect ratio  $\varepsilon$ . In this section, the aspect ratio  $\varepsilon$  which reflects the momentum distribution of the viscous flow is varied (Table 3).

Figures 9a and 9b show the normal and tangential forces induced on a flexible barrier, with stiffness 1  $k_c$ , by debris flows with aspect ratios  $\varepsilon$  varied from 0.019 to 0.023 (Table 5). A slight change in  $\varepsilon$  can induce up to 20% increase in the normal impact force. The peak normal impact force and tangential force are normalized by the

Height Froude number <i>Fr</i> <sub>h</sub>	Length Froude number <i>Fr</i> 1	Aspect ratio $\varepsilon$	Normal F <sub>peak</sub> (kN)	Normal F <sub>static</sub> (kN)	Tangential $F_{\rm peak}$ (kN)	Normalized normal $F_{\rm peak}$	Normal $F_{ m peak}/F_{ m static}$	Normalized tangential $F_{\rm peak}$
3.67	0.501	0.019	749	430	430	1.00	1.74	1.00
3.59	0.512	0.020	789	445	445	1.05	1.77	1.03
3.62	0.538	0.022	883	451	469	1.18	1.96	1.09
0.56	0.545	0.000	000	450	101	1.00	0.00	1 10

**Table 5** Summary of flexible barrier response under different aspect ratio (all dimensions in prototype)

corresponding forces of viscous flow with  $\varepsilon$  = 0.019 (Figure 14). Results show that an increasing  $\varepsilon$  leads to higher normal and tangential cable forces. These trends demonstrate an increasing contribution of concentrated frontal momentum as the flow front thickens upon impact. Higher aspect ratio means a higher flow depth h, higher impact area hL, and thus higher impact force  $F = \alpha \rho v^2 hL$  on flexible barrier. The term  $\alpha \rho v^2 hL$  actually can also be regarded as the frontal momentum flux passing through the cross section where the flexible barrier is installed.

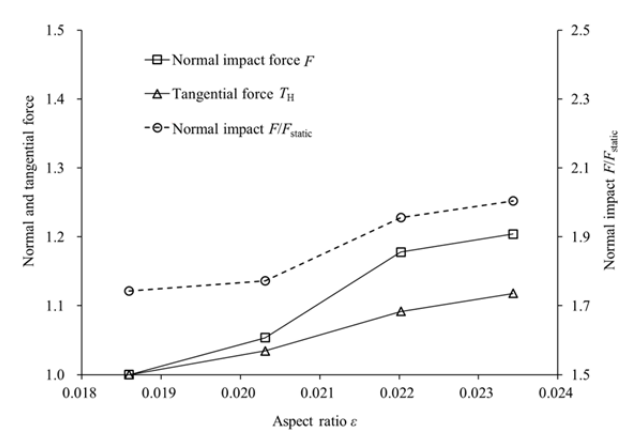


**Figure 14** Influence of aspect ratio  $\varepsilon$  on the normal, tangential forces, and the peak-static force ratio.

The aspect ratio  $\varepsilon$  also helps to explain the low sensitivity of normal impact force exhibited by the flexible barrier upon debris impact in Figure 13a. No matter how the barrier stiffness varies and how the barrier deflects, the debris flow with a low aspect ratio carries limited amount of momentum at the flow front and hence can only impost limited impact force on the flexible barrier. As a result, the limited frontal impact is further covered by the gradual accumulation (static load) subsequent flow. The large barrier deflection might mainly be caused by the static load, not the dynamic frontal impact load. The limited impact force is reflected by the low peak-static force ratio (about 1.1; Figure 14) at  $\varepsilon$  = 0.019, leaving no space (10% of the static load) for the flexible barrier to attenuate. Contrary to the low sensitivity of normal impact load in this study, the two-phase (sand-liquid mixture) impact on rigid and flexible barriers carried out by Song et al. (2018) clearly demonstrated the barrier stiffness effect. The normal load on the flexible barrier could be 50% lower than that on the rigid barrier. Note that the two-phase flows were characterized as surge flows (high aspect ratio). This in turn elaborates that the debris-barrier stiffness could affect the normal impact load, as long as the flows are featured as high aspect ratio.

Natural debris flows differ from near-source debris flows carried out in physical modelling because natural flows can travel up to several kilometers away from their point of initiation (Major 1997). Before impacting structures, debris flows elongates and only have limited flow thickness and this in turn influences the frontal impact. As a result, the thin flow layers and deposits on top of each other over a long period of time and develops a deposit where the static load dominates instead of the dynamic component. A well-documented case portraying this phenomena is the Illgraben Torrent on 18th May 2006 (Wendeler et al. 2007). The debris flow event had an estimated volume of 15000 m3, density of around 1600 kg/m<sup>3</sup>, and was intercepted by a flexible barrier installed along its flow path. The distance between the point of initiation and the flexible barrier was about 13 km (Berger et al. 2011) and the loading duration on the flexible barrier was about 120 s. From the time histories of the instrumented cables and the flow depth measurements, debris loading was predominantly quasi-static loading and the frontal impact was fully covered by the large amount of accumulated debris from the subsequent flow.

With the assistance of numerical tools (e.g., Hungr 1995; Kwan and Sun 2006), estimation of the macroscopic debris flow parameters, (e.g., flow velocity, flow depth, and flow length) and estimation of the related dimensionless indices, (e.g., Froude number  $Fr_h$  and flow aspect ratio  $\varepsilon$ ), are generally

not difficult problem. The height Froude number  $Fr_h$  is currently adopted in the engineering design (Hübl et al. 2009) and the scaling of the length l (aspect ratio  $\varepsilon$ ) is not explicitly considered. Under the circumstance of an extremely elongated debris flow event, it may be appropriate to only consider the static load on the barrier. However, more experimental and field monitoring data is needed to quantify the range of aspect ratios relevant for a design relying mostly on static loading.

#### 7 Conclusions

Numerical back-analysis and a parametric study were carried out to study the effects of distributed debris flow and concentrated boulder impact on the dynamic response of a flexible barrier with different cable stiffness. New force approach, based on the stiffness number and aspect ratio, to determine the impact force induced by debris flows on flexible barrier is proposed. Findings are drawn as follows:

- 1) The normal impact force exerted by a debris flow is not sensitive to the stiffness of the flexible barrier because the momentum in a debris flow rapidly diminishes via internal and boundary shearing. However, this finding only applies to the flows with low aspect ratios. As long as the flow is featured with high aspect ratio (surge flow, Song et al. 2018), the impact load of fine debris on flexible barrier could also be affected by the barrier stiffness. By contrast, the impact force generated by boulder impact is highly sensitive to the stiffness of the barrier. Different from the progressive and distributed loading of debris with dead zone forming at the base, the concentrated momentum of boulder impact is mainly attenuated by the flexible barrier itself.
- 2) Both stiffness of debris and stiffness of boulder influence the distinct response of flexible barrier. The equivalent stiffness is proposed to characterize the impact between a debris flow or boulder, and a flexible barrier. The equivalent stiffness of debris collapses into a narrow range, denoting that the high compliance of debris controls the equivalent stiffness for debris-barrier interaction. The narrow range of debris-barrier stiffness also helps to explain the insensitivity of normal impact force. While the equivalent stiffness

of boulder covers a wide range of stiffness number, about 10 times of that of debris impact, indicating that both properties of boulder and barrier control the dynamic barrier response under boulder impact.

- 3) Due to the effect of geometry, the tangential force induced on a flexible barrier cable by debris flows and boulders is highly sensitive to barrier stiffness. The tangential cable force can be reduced by allowing larger deflection. A lower barrier stiffness facilitates larger barrier deflection and deflection angle. The tangential component of the cable force is reduced accordingly, even though the normal impact force remains constant. With the stiffness ranging from 1 to 80  $k_c$ , the tangential force for viscous debris impact is increased three times. By providing a lower stiffness and long braking displacement of flexible barrier, the larger deflection angle will effectively control the amount of tangential component mobilized.
- 4) Only when the flow is characterized as high aspect ratio, the effect of flexible barrier stiffness could be exhibited. The aspect ratio quantifies the flow shape and momentum distribution along the flow length and has generally been neglected in the engineering design. The relationship between the aspect ratio and normal impact force shows that a minor change in aspect ratio (0.019 to 0.023) induces a 20% increase in normal impact force. Under the circumstance of an extremely elongated debris flow event, a decoupled analysis, which only considers the static load on the barrier, should be enough for the flexible barrier design.

### Acknowledgements

The authors acknowledge the support from the National Natural Science Foundation of China (Grant Nos. 51809261, 11672318, and 51709052). The authors would also like to acknowledge the financial support from the Theme-based Research Grant T22-603/15N and the General Research Fund 16209717 provided by the Research Grants Council of the Government of Hong Kong SAR, China. Finally, the authors are grateful for the financial support by the Hong Kong Jockey Club Disaster Preparedness and Response Institute (HKJCDPRI18EG01).

Electronic supplementary material: Supplementary material (Appendixes 1-2) are available in the online version of this article at https://doi.org/10.1007/s11629-018-5314-6

#### References

- AECOM (2012) Detailed Study of the 7 June 2008 Landslides on the Hillside above Yu Tung Road, Tung Chung (GEO Report No. 271). Geotechnical Engineering Office, Hong Kong SAR Government.
- Armanini A, Larcher M, Odorizzi M (2011) Dynamic impact of a debris flow front against a vertical wall. In: Proceedings of the 5th International Conference on Debris-Flow Hazards Mitigation: Mechanics, Prediction and Assessment. Padua, Italy, pp 1041-1049.
- ARUP (2013) Pilot Numerical Investigation of the Interactions between Landslide Debris and Flexible Debris-resisting Barriers. Report prepared for Geotechnical Engineering Office, Hong Kong SAR Government. ARUP (Hong Kong).
- Ashwood W, Hungr O (2016) Estimating the total resisting force in a flexible barrier impacted by a granular avalanche using physical and numerical modeling. Canadian Geotechnical Journal 53(10): 1700-1717.

https://doi.org/10.1139/cgj-2015-0481

- Austrian Standards Institute (2010) ONR 24801. Protection works for torrent control: Static and dynamic loads (impacts), Vienna (in German).
- Berger C, McArdell BW, Schlunegger F (2011) Direct measurement of channel erosion by debris flows, Illgraben, Switzerland. Journal of Geophysical Research: Earth Surface 116(F1). https://doi.org/10.1029/2010JF001722
- Blanco-Fernandez E, Castro-Fresno D, del Coz Diaz JJ, et al. (2016) Flexible membranes anchored to the ground for slope stabilisation: Numerical modelling of soil slopes using SPH. Computers and Geotechnics: 78: 1-10.

https://doi.org/10.1016/j.compgeo.2016.04.014

- Bowman ET, Laue J, Imre B, et al. (2010) Experimental Modelling of Debris Flow Behaviour Using a Geotechnical Centrifuge. Canadian Geotechnical Journal 47(7): 742-762. https://doi.org/10.1139/T09-141
- Brighenti R, Segalini A, Ferrero AM (2013) Debris flow hazard mitigation: a simplified analytical model for the design of flexible barriers. Computers and Geotechnics 54: 1-15. https://doi.org/10.1016/j.compgeo.2013.05.010
  Bugnion L, Wendeler C (2010) Shallow landslide full-scale
- Bugnion L, Wendeler C (2010) Shallow landslide full-scale experiments in combination with testing of a flexible barrier. WIT Transactions on Engineering Sciences 67:161-173. https://doi.org/10.2495/DEB100141
- Canelli L, Ferrero AM, Migliazza M, et al. (2012) Debris flow risk mitigation by the means of rigid and flexible barriersexperimental tests and impact analysis. Natural Hazards and Earth System Sciences 12: 1693-1699.

https://doi.org/10.5194/nhess-12-1693-2012

- Castanon-Jano L, Blanco-Fernandez E, Castro-Fresno D, et al. (2017) Energy dissipating devices in falling rock protection barriers. Rock Mechanics and Rock Engineering 50(3): 603-610 https://doi.org/10.1007/s0060
- 619. https://doi.org/10.1007/s0060
  Chan SL, Zhou ZH, Liu YP (2012) Numerical Analysis and Design of Flexible Barriers Allowing for Sliding Nodes and Large Deflection Effects. In: CK Lau, E Chan and J Kwan (eds). In: Proceedings of the One Day Seminar on Natural Terrain Hazards Mitigation Measures, Hong Kong. The Association of Geotechnical and Geoenvironmental Specialists (Hong Kong) Limited. pp 29–43.
- Chen HX, Zhang LM Zhang S, et al. (2013) Hybrid simulation of the initiation and runout characteristics of a catastrophic debris flow. Journal of Mountain Science 10(2): 219-232. https://doi.org/10.1007/s11629-013-2505-z
- Choi CE, Au-Yeung SCH, Ng CWW, et al. (2015) Flume

- investigation of landslide granular debris and water runup mechanisms. Géotechnique Letters 5(1): 28-32. https://doi.org/10.1680/geolett.14.00080
- DeNatale JS, Iverson RM, Major JJ, et al. (1999) Experimental testing of flexible barriers for containment of debris flows. US Department of the Interior, US Geological Survey.
- Donea J, Giuliani S, Halleux JP (1982) An arbitrary Lagrangian-Eulerian finite element method for transient dynamic fluidstructure interactions. Computer methods in applied mechanics and engineering 33(1-3): 689-723.
- https://doi.org/10.1016/0045-7825(82)90128-1
  EOTA. 2016. Flexible Kits for Retaining Debris Flows and Shallow Landslides/Open Slope Debris Flows. EAD340020-00-0106. Available online at: https://www.eota.eu/handlers/download.ashx?filename=ead-in-ojeu%2fead-340020-00-0106-ojeu2016.pdf (Accessed on 19 June 2019)
- Faug T (2015) Macroscopic force experienced by extended objects in granular flows over a very broad Froude-number range. European Physical Journal E 38(24): 1-10. https://doi.org/10.1140/epje/i2015-15034-3
- GEO (2012) Technical Guidelines on Empirical Design of Flexible Barriers for Mitigating Natural Terrain Open Hillslope Landslide Hazards. Guidance Note No. 37 (TGN 37). Geotechnical Engineering Office, HKSAR Government. Available online at: https://www.cedd.gov.hk/eng/publications/guidance\_notes/doc/TGN37.pdf (Accessed on 19 June 2019)
- Hallquist JO (2007) LS-DYNA keyword user's manual. Livermore Software Technology Corporation. p 970.
- Huebl J, Nagl G, Suda J, et al. (2017) Standardized Stress Model for Design of Torrential Barriers under Impact by Debris Flow (According to Austrian Standard Regulation 24801). International Journal of Erosion Control Engineering 10(1): 47-55. https://doi.org/10.13101/ijece.10.47
- Hübl J, Suda J, Proske D, et al. (2009) Debris flow impact estimation. In: Proceedings of the 11th International Symposium on Water Management and Hydraulic Engineering, Ohrid, Macedonia. pp 1-5.
- Hungr O (1995) A model for the runout analysis of rapid flow slides, debris flows, and avalanches. Canadian Geotechnical Journal 32(4): 610-623. https://doi.org/10.1139/t95-063
- Hungr O (2008) Simplified models of spreading flow of dry granular material. Can Geotech J 45(8): 1156–1168.

https://doi.org/10.1139/To8-059

- Ishikawa N, Inoue R, Beppu M, et al. (2010) Dynamic load characteristics of debris flow model using different gravel size distribution. In: Proceedings of INTERPRAEVENT. pp 207-216.
- Iverson RM (1997) The physics of debris flows. Reviews of geophysics 35(3): 245-296. https://doi.org/10.1029/97RG00426
- Iverson RM, Logan M, Denlinger RP (2004) Granular avalanches across irregular three dimensional terrain: 2. Experimental tests. Journal of Geophysical Research: Earth Surface 109(F1). https://doi.org/10.1029/2003JF000084
- Iverson RM (2015) Scaling and design of landslide and debrisflow experiments. Geomorphology 244: 9-20.
- https://doi.org/10.1016/j.geomorph.2015.02.033

  Iverson RM, George DL (2014) A depth-averaged debris-flow model that includes the effects of evolving dilatancy. I. Physical basis. Proceedings of the Royal Society of London A: Mathematical, Physical and Engineering Sciences 470(2170): 20130819. https://doi.org/10.1098/rspa.2013.0819

- Johnson KL (1985) Contact mechanics. Cambridge University
- Johnson CG, Kokelaar BP, Iverson RM, et al. (2012) Grain-size segregation and levee formation in geophysical mass flows. J Geophys Res 117: F002185.

https://doi.org/10.1029/2011JF002185

(Accessed on 19 June 2019)

- Koo RCH (2017) Mechanisms of interaction between dry sand flow and multiple rigid barriers: Flume and finite-element modelling. PhD Thesis. The Hong Kong University of Science and Technology
- Kwan JSH (2012) Supplementary Technical Guidance on Design of Rigid Debris-resisting Barriers. GEO Report No. 270. Geotechnical Engineering Office, HKSAR Government. https://www.cedd.gov.hk/eng/ Available online at: publications/geo\_reports/doc/er270/er270links.pdf
- Kwan JSH, Chan SL, Cheuk JCY, et al. (2014) A case study on an open hillside landslide impacting on a flexible rockfall barrier at Jordan Valley, Hong Kong. Landslides 11(6): 1037-1050. https://doi.org/10.1007/s10346-013-0461-x
- Kwan JSH, Koo RCH, Ng CWW (2015) Landslide mobility analysis for design of multiple debris-resisting barriers. Canadian Geotechnical Journal 52(9): 1345-1359. https://doi.org/10.1139/cgj-2014-0152
- Kwan JSH, Sun H W (2006) An improved landslide mobility model. Canadian Geotechnical Journal 43(5): 531-539. https://doi.org/10.1139/t06-010
- Leonardi A, Wittel FK, Mendoza M, et al. (2016) Particle-Fluid-Structure Interaction for Debris Flow Impact on Flexible Barriers. Computer-Aided Civil and Infrastructure Engineering 31: 323-333. https://doi.org/10.1111/mice.12165
- Ma C, Hu K, Tian M (2013) Comparison of debris-flow volume and activity under different formation conditions. Natural hazards 67(2): 261-273.

https://doi.org/10.1007/s11069-013-0557-6

- Major JJ (1997) Depositional processes in large scale debris flow experiments. The Journal of Geology 105(3): 345-366.
- Moriguchi S, Borja RI, Yashima A, et al. (2009) Estimating the impact force generated by granular flow on a rigid obstruction. Acta Geotechnica 4(1): 57-71.

- https://doi.org/10.1007/\$11440-009-0084-5 Ng CWW, Song D, Choi CE, et al. (2016a) A novel flexible barrier for landslide impact in centrifuge. Géotechnique Letters 6(3): 221-225.
  - https://doi.org/10.1680/jgele.16.00048
- Ng CWW, Song D, Choi CE, et al. (2016b) Impact mechanisms of granular and viscous flows on rigid and flexible barriers. Canadian Geotechnical Journal 54(2): 188-206.
- https://doi.org/10.1139/cgj-2016-0128 Randolph MF, White DJ (2012) Interaction forces between pipelines and submarine slides-A geotechnical viewpoint. Ocean Engineering 48: 32-37.

https://doi.org/10.1016/j.oceaneng.2012.03.014

- Sasiharan N, Muhunthan B, Badger TC, et al. (2006) Numerical analysis of the performance of wire mesh and cable net rockfall protection systems. Engineering geology 88(1): 121-132. https://doi.org/10.1016/j.enggeo.2006.09.005
- Schofield AN (1980) Cambridge geotechnical centrifuge operations. Geotechnique 30(3): 227-268.
- Shen W, Zhao T, Zhao J, et al. (2018). Quantifying the impact of dry debris flow against a rigid barrier by DEM analyses.

- Engineering Geology 241: 86-96.
- https://doi.org/10.1016/j.enggeo.2018.05.011
- Song D, Choi CE, Ng CWW, et al. (2018) Geophysical Flows Impacting a Flexible Barrier: Effects of Solid-fluid Interaction. Landslides 15(1): 99-110.

https://doi.org/10.1007/s10346-017-0856-1

Song D, Zhou GGD, Xu M, Choi CE, Li S, Zheng Y (2019) Quantitative analysis of debris-flow flexible barrier capacity from momentum and energy perspectives. Engineering Geology 251: 81-92.

https://doi.org/10.1016/j.enggeo.2019.02.010

- Take WA (2015) Thirty-Sixth Canadian Colloquium: Advances in visualization of geotechnical processes through digital image correlation. Canadian Geotechnical Journal 52(9): 1199-1220. https://doi.org/10.1139/cgj-2014-0080
- Utili S, Zhao T, Houlsby G T (2015) 3D DEM investigation of granular column collapse: evaluation of debris motion and its destructive power. Engineering geology 186: 3-16. https://doi.org/10.1016/j.enggeo.2014.08.018
- Vagnon F, Segalini A (2016) Debris flow impact estimation on a rigid barrier. Natural Hazards and Earth System Sciences 16(7): 1691-1697.

- https://doi.org/10.5194/nhess-16-1691-2016 Wendeler C (2008) Murgangrückhalt in Wildbächen: Grundlagen zu Planung und Berechnung von flexiblen Barrieren. Doctoral dissertation (in German), ETH Zurich. No. 17916.
- Wendeler C, McArdell BW, Rickenmann D, et al. (2006) Field testing and numerical modeling of flexible debris flow barriers. In: Proceedings of the Sixth International Conference of Physical Modelling in Geotechnics, Hong Kong. pp 4-6.
- Wendeler C, Volkwein, A, Roth A, et al. (2007) Field measurements and numerical modelling of flexible debris flow barriers. In: Debris-Flow Hazards Mitig. Mech. Predict. Assess. Millpress, Rotterdam. pp 681-687.
- Wendeler C, Volkwein A (2015) Laboratory tests for the optimization of mesh size for flexible debris-flow barriers. Natural Hazards & Earth System Sciences 15(12): 2597-2604. https://doi.org/10.5194/nhess-15-2597-2015
- Wendeler C (2016) Debris flow protection systems for mountain torrents - basic principles for planning and calculation of flexible barriers. WSL Bericht 44. ISSN 2296-3456.
- White DJ, Take WA, Bolton MD (2003) Soil deformation measurement using particle image velocimetry (PIV) and photogrammetry. Geotechnique 53(7): 619-631. https://doi.org/10.1680/geot.2003.53.7.619
- WSL (2009) Full-scale Testing and Dimensioning of flexible barriers. Technical report 1-22. WSL, debris flow Birmensdorf.
- Zhang S (1993) A comprehensive approach to the observation and prevention of debris flows in China. Natural Hazards 7(1): 1-23. https://doi.org/10.1007/BF00595676
- Zhou ZH, Liu YP, Chan SL (2011) Nonlinear finite element analysis and design of flexible barrier, Project Report. The Hong Kong Polytechnic University, Hong Kong SAR.
- Zhou GGD, Ng CWW (2010) Numerical investigation of reverse segregation in debris flows by DEM. Granular matter 12(5): 507-516. https://doi.org/10.1007/s10035-010-0209-4

The following Appendixes (Appendixes 1-2) are the Electronic Supplementary Material of the article entitled "Debris flow impact on flexible barrier: effects of debris-barrier stiffness and flow aspect ratio" at https://doi.org/10.1007/s11629-018-5314-6

The maximum deflection D and forces of a single cable under boulder induced concentrated normal impact force F (Figure 1a of the main text) and the debris induced distributed normal line load pL = F (Figure 1b of the main text) are discussed. For simplicity, a cable with single linear stiffness  $nk_c$  is assumed, where  $k_c$  is the reference cable stiffness (N/m) and n ranges from 0.5 to 80 in this study. The varying stiffness of the flexible barrier cable can be provided by the brake (energy dissipating) elements attached at the end of cable.

#### Appendix 1 Deflection and forces under concentrated loading

The elongation  $\Delta L$  of cable with initial length L under concentrated normal load F

$$\Delta L = \frac{T}{nk_c} = \frac{F}{nk_c} \frac{1}{2\sin\psi} \tag{A.1}$$

where, *T* is cable force, and  $\psi$  is the deflection angle.

By trigonometry of the elongated cable

$$\cos \psi = \frac{L}{L + \Delta L} \tag{A.2}$$

Substitute Eq. (A.1) into Eq. (A.2)

$$\cos \psi + \frac{F_{\rm N}}{2 \tan \psi} = 1 \tag{A.3}$$

where,  $F_N = F/(nk_cL)$ , is a concentrated impact load by the combination of initial length L and stiffness  $nk_c$ . The normalized maximum deflection  $D_N = D/(L/2)$  by half of the initial cable length L/2

$$D_{\rm N} = \tan \psi \tag{A.4}$$

Based on Eq. (A.3) and (A.4), the load-deflection ( $F_N$ - $D_N$ ) relationship

$$F_{\rm N} = 2D_{\rm N} - \frac{2D_{\rm N}}{\sqrt{1 + D_{\rm N}^2}} \tag{A.5}$$

The induced force along the cable, normalized cable force  $T_{\rm N}$ 

$$T_{\rm N} = \frac{T}{nk_{\rm c}L} = \frac{F_{\rm N}}{2\sin\psi} \tag{A.6}$$

The horizontal component of total cable force  $T_N$ , normalized  $T_{HN}$ , is tangential to the barrier face

$$T_{\rm HN} = \frac{T_{\rm H}}{nk_{\rm c}L} = \frac{F_{\rm N}}{2\tan\psi} \tag{A.7}$$

The normal component  $T_{\rm IN}$  equilibrates the concentrated force  $F_{\rm N}$ 

$$T_{\rm IN} = \frac{T_{\rm I}}{nk_c L} = \frac{F_{\rm N}}{2} \tag{A.8}$$

#### Appendix 2 Deflection and forces under distributed loading

Since the debris is always compliant with the cable and the pressure is perpendicular to the cable, a circular curve is the best approximation of the deformed cable under distributed load (Figure 1b of the main text, Sasiharan et al. 2006).

The pressure p on a circular line can be decomposed into uniform p across the initial length L and uniform p along the deflection p. Note most literatures assume only the horizontally distributed p on the initial length p (approximated as a parabola or catenary curve) and the vertical component is neglected. This assumption is acceptable for the impact with minor deflection and is nontrivial as the deflection keeps increasing. The cable force p is not uniform for a distributed loading case with the uniform p along the deflection direction. Here the brake element p is assumed to be connected at the cable end.

The arc length S of a whole circular line under distributed load, with its horizontal component pL = F

$$S = L + \frac{T}{nk_c} = L + \frac{pr}{nk_c} \tag{B.1}$$

where, r is the radius of the circle.

The arc length S can also the deduced from the definition of a circle circumference

$$S = \frac{2\psi}{180}\pi r \tag{B.2}$$

Hence

$$L + \frac{pr}{nk_c} = \frac{2\psi}{180}\pi r \tag{B.3}$$

$$1 + \frac{F}{nk_{o}L}\frac{r}{L} = \frac{\pi}{180}\psi \frac{2r}{L}$$
 (B.4)

Since  $\sin \psi = \frac{L}{2r}$ ,

$$1 + \frac{F}{nk_c L} \frac{2r}{2L} = \frac{\pi}{180} \arcsin(\frac{L}{2r}) \frac{2r}{L}$$
 (B.5)

$$1 + F_{\rm N} \frac{1}{2x} = \frac{\pi}{180} \arcsin(x) \frac{1}{x}$$
 (B.6)

where  $F_N = F/(nk_cL)$ , is a normalized impact load by the combination of initial cable length L and stiffness  $nk_c$ . x = L/(2r) =  $\sin \psi$  is a non-dimensionalzed variable that helps to solve the deflection angle  $\psi$ .

The maximum deflection  $D_N$  of can be determined as follows

$$D = r(1 - \cos \psi) \tag{B.7}$$

$$D_{\rm N} = \frac{D}{L/2} = \frac{(1 - \cos \psi)}{\sin \psi} \tag{B.8}$$

Eqs. (B6) and (B8) characterize the load-deflection ( $F_N$ - $D_N$ ) relationship of the distributed loading. The normalized normal component  $T_1$  (normal impact force) at the cable end

$$T_{\rm IN} = \frac{T_{\rm I}}{nk_{\rm o}L} = \frac{F_{\rm N}}{2} \tag{B.9}$$

The total cable force  $T_N$  at the cable end

$$T_{\rm N} = \frac{T}{nk_{\rm c}L} = \frac{F_{\rm N}}{2\sin\psi} \tag{B.10}$$

The normalized horizontal component  $T_{\rm HN}$  (tangential force) at the cable end

$$T_{\rm HN} = T_{\rm N} \cos \psi = \frac{F_{\rm N}}{2 \tan \psi} \tag{B.11}$$

The cable force T is not uniform for a distributed loading case because of the uniform p along the deflection direction. The normalized horizontal component  $T_{HN}$  in the middle of cable

$$T'_{\rm HN} = T_{\rm HN} + F_{\rm N}D_{\rm N} \tag{B.12}$$

The relationship between maximum deflection  $D_N$  and impact load  $F_N$  for the distributed loading is shown in Figure A. Different from the  $F_N$  in Eq.(B6), the impact load is normalized by  $k_cL$ . As expected, the deflection  $D_N$  of the cable decreases with the increasing cable stiffness  $nk_c$ .

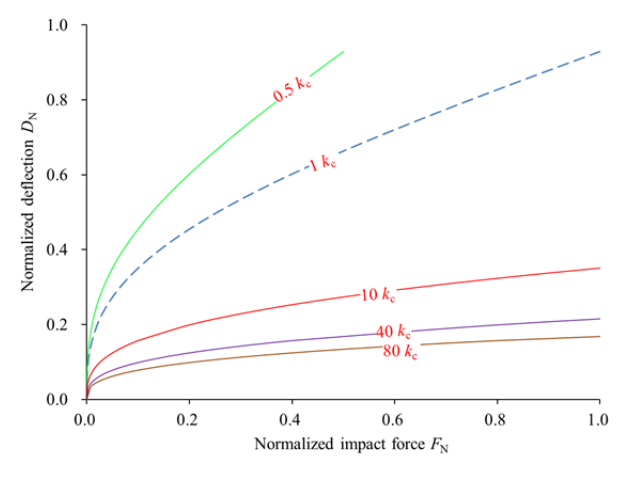


**Figure A** Relationship between the impact load and the maximum deflection. A plot normalized by  $nk_cL$  is shown in Figure 2a of the main text.